Applied Organometallic Chemistry

WILEY

Applied Organometallic Chemistry

RESEARCH ARTICLE OPEN ACCESS

Heterobimetallic Pd-Ru Catalysts for the Synthesis of Functionalized Polynorbornenes via Reductive Heck/ROMP Reactions

Thais R. Cruz[1,2] | Juliana I. P. Maia[3] | Pedro I. S. Maia[3] | Antonio E. H. Machado[4,5] | Beatriz E. Goi[1] | Lionel Delaude[2] | Valdemiro P. Carvalho-Jr[1]

[1]São Paulo State University (Unesp), School of Technology and Sciences, Presidente Prudente, SP, Brazil | [2]Laboratory of Catalysis, Institut de Chimie Organique (B6a), Allée du six Août 13, Université de Liège, Liège, Belgium | [3]Instituto de Ciências Exatas, Naturais e Educação, Universidade Federal do Triângulo Mineiro, Uberaba, Minas Gerais, Brazil | [4]Instituto de Química, Universidade Federal de Uberlândia, Uberlândia, Minas Gerais, Brazil | [5]Programa de Pós-Graduação em Ciência e Engenharia de Materiais, Universidade Federal de Catalão, Catalão, Goiás, Brazil

Correspondence: Lionel Delaude (l.delaude@uliege.be) | Valdemiro P. Carvalho-Jr (valdemiro.carvalho@unesp.br)

Received: 30 May 2025 | **Revised:** 21 August 2025 | **Accepted:** 30 August 2025

Funding: This work was supported by the Fundação de Amparo à Pesquisa do Estado de São Paulo (2021/13128-1, 2021/11873-1), Conselho Nacional de Desenvolvimento Científico e Tecnológico (311747/2023-0, 88881.690136/2022-01), and Fundação de Amparo à Pesquisa do Estado de Minas Gerais (RED-00116-23).

Keywords: bifunctional catalysts | olefin metathesis | palladium | ruthenium | thiosemicarbazide ligands

ABSTRACT

Heterobimetallic complexes offer greater versatility for applications in homogeneous catalysis than their monometallic counterparts. To take advantage of this synergy, three [Pd(*N,N,S*-TSC)(4-NH_2Py)] complexes (**mono-Pd^{Me}**, **mono-Pd^{Me,Me}** and **mono-Pd^{Ph}**) were synthesized from [$PdCl_2$(MeCN)$_2$] and appropriate thiosemicarbazide (TSC) ligand precursors, followed by the addition of 4-aminopyridine (4-NH_2Py). The reaction of these mono-Pd^{L} complexes with [$RuCl_2$(η^6-*p*-cymene)]$_2$ then afforded three heterobimetallic complexes with the generic formula [{$RuCl_2$(*p*-cymene)}-μ-{(4-NH_2Py)Pd (TSC)}] (**Ru-Pd^{Me}**, **Ru-Pd^{Me,Me}** and **Ru-Pd^{Ph}**). All these novel compounds were characterized by elemental analysis, spectroscopic techniques, cyclic voltammetry, and density functional theory (DFT) calculations. The molecular structure of **mono-Pd^{Me}** was determined by X-ray diffraction analysis. The Ru-Pd^{L} complexes were evaluated as bifunctional catalysts in the reductive Heck coupling of norbornadiene (NBD) with iodobenzene and the ring-opening metathesis polymerization (ROMP) of phenylnorbornene (Ph-NBE). They were very active for the reductive Heck reaction, reaching yields higher than 90% when a [Pd]/[NBD]/[PhI] ratio of 1/418/1344 was employed at 120°C. Upon activation with ethyl diazoacetate (EDA), they were also able to polymerize Ph-NBE with yields around 70% using a [Ph-NBE]/[Ru-Pd^{L}] ratio of 3000 at 50°C for 30 min. The **Ru-Pd^{Me,Me}** complex showed the highest activity in the ROMP of Ph-NBE and was successfully applied for mediating the synthesis of poly (Ph-NBE) from NBD via tandem catalysis.

1 | Introduction

Efficient and sustainable catalysts are crucial for modern chemistry, as they play a key role in the vast majority of industrial or laboratory-scale transformations that are used for the synthesis of commodity chemicals, pharmaceutical drugs, or polymeric materials, to name just a few [1–3]. Among the various classes of catalysts available to date, mononuclear transition metal complexes have long been recognized as versatile and effective promoters for a wide range of organic reactions, due to their unique

properties, such as well-defined coordination environments, tunable redox potentials, and the ability to trigger various reaction mechanisms [4, 5].

Although they have been less investigated so far, heterobimetallic complexes can further enhance the catalytic abilities of their monometallic counterparts through the synergistic interplay between the two metal centers, each contributing distinctive functionalities and redox properties for activating diverse substrates and facilitating bond-breaking and bond-forming processes [6–10]. These improvements stem from factors like cooperative substrate binding, electron transfer between metal centers, and stabilization of reaction intermediates. For instance, the combination of late and early transition metals has proven effective in C–H activation reactions. The late transition metal facilitates the cleavage of C–H bonds, while the early transition metal stabilizes the resulting alkyl or aryl species [11]. Heterobimetallic complexes have also shown promise for palladium-catalyzed cross-coupling reactions, such as the Heck reaction. In this case, a Pd-based moiety catalyzes the coupling of an aryl halide with an alkene, while a Cu-based unit facilitates the regeneration of the active Pd species. The cooperative action of the two metals enables an efficient and selective formation of substituted alkenes [12]. In the field of olefin metathesis, Dias and Grubbs have demonstrated the superior catalytic performance of heterobimetallic ruthenium-based systems, where the incorporation of a second metal center, such as Rh or Os, enhances activity through electronic and steric effects. This interplay leads to improved efficiency and selectivity in the ring-opening metathesis polymerization (ROMP) of cycloolefins, expanding the scope of metathesis-based polymer synthesis [13].

Research carried out in our laboratory has shown that the ROMP of norbornene and norbornadiene could be initiated using non-carbene, amine-based ruthenium complexes provided that ethyl diazoacetate (EDA) was added to generate active alkylidene species in situ [14–17]. Recently, we also reported the synthesis of heterobimetallic Ni-Ru and Pd-Ru systems for multifunctional polymerization catalysis [18–20]. Herein, we disclose the synthesis and characterization of novel heterobimetallic Pd-Ru complexes and their use to mediate reductive Heck and ROMP reactions in a sequential one-pot process. These catalysts were designed to combine a palladium-thiosemicarbazide (TSC) moiety to promote the reductive cross-coupling of norbornadiene and an aryl halide, together with a ruthenium-arene unit to initiate the ROMP of the resulting 5-phenylnorbornene monomer. In addition, the corresponding monometallic Pd-TSC and Ru-arene species were also prepared, and their catalytic activities evaluated to better assess the contribution of each metal center to the overall transformation.

2 | Experimental

2.1 | General Information

Unless otherwise specified, all the syntheses were carried out under a normal atmosphere. The $[PdCl_2(MeCN)_2]$ complex was prepared according to literature [21]. The $[RuCl_2(\eta^6\text{-}p\text{-cymene})]_2$ dimer, norbornene (NBE), norbornadiene (NBD), ethyl diazoacetate (EDA), 4-aminopyridine (4-NH_2Py), diacetyl monoxime, 4-methyl-3-thiosemicarbazide, 4,4-dimethyl-3-thiosemicarbazide, 4-phenylthiosemicarbazide, chlorobenzene, bromobenzene, iodobenzene, triethylamine (Et_3N), ethyl acetate, hexane, and silica gel were purchased from Aldrich or TCI and used as received. Elemental analyses were performed on a PerkinElmer CHN 2400 instrument. FT-IR spectra were recorded on a PerkinElmer Frontier instrument equipped with a diamond ATR module. UV–Vis spectra were recorded on a Shimadzu UV-1800 spectrophotometer using 1-cm-path length quartz cells in DMSO at 25°C. ^{1}H and $^{13}C\{^1H\}$ NMR spectra were recorded in DMSO-d_6 at 298 K on a Bruker DRX 400 spectrometer operating at 400.13 and 100.62 MHz, respectively. Chemical shifts are listed in ppm downfield from TMS and referenced from the solvent peaks or TMS. The signals were labeled as s = singlet, d = doublet, dd = doublet of doublets, t = triplet, and sept = septet. GC analyses were performed on a Varian Star 3400 CX gas chromatograph equipped with an RSLM-150 capillary column (25 m × 0.25 mm, 0.25-μm film thickness) and a flame ionization detector. Electrochemical measurements were performed in CH_2Cl_2 with 0.1 M n-Bu_4NPF_6 at 25°C ± 0.1°C using an Autolab PGSTAT204 potentiostat with a glassy carbon and platinum wire as working and auxiliary electrodes, respectively. The reference electrode was glassy carbon.

2.2 | Synthesis of the Thiosemicarbazide Ligand Precursors

The ligand precursors $\mathbf{H_2L^{Me}}$, $\mathbf{H_2L^{Me,Me}}$, and $\mathbf{H_2L^{Ph}}$ were synthesized according to a procedure adapted from the literature [22]. To a solution of diacetyl monoxime (8.0 mmol) in a 2/3 v/v mixture of EtOH and H_2O (10 mL), a thiosemicarbazide (8.0 mmol) in EtOH (10 mL) was added, followed by acetic acid (0.5 mL). The reaction mixture was stirred and refluxed for 4 h. After cooling to room temperature, the colorless precipitate was filtered, washed with n-hexane, and dried under reduced pressure. It was recrystallized from ethanol.

2.2.1 | 3-(Hydroxyimino)butan-2-ylidene)-*N*-methylhydrazine-1-carbothioamide ($\mathbf{H_2L^{Me}}$)

Colorless crystals (1.25 g, 83% yield). Anal. calcd for $C_6H_{12}N_4OS$ (188.07): C, 38.28; H, 6.43; N, 29.76; S, 17.03%. Found: C, 38.32; H, 6.47; N, 29.84; S, 17.08%. FT-IR (ATR): $\bar{\nu}$ 3353 (O–H), 3294, 3205 (N–H), 1544 $(C{=}N)_{tsc}$, 1498 $(C{=}N)_{ox}$, 1363 δ(O–H), 1005 (N–O), 829 cm^{-1} (C=S). UV–Vis: λ_{max} (ε_{max}): 301 nm (49,500 $M^{-1}cm^{-1}$). ^{1}H NMR (400 MHz, DMSO-d_6,): δ 11.54 (s, 1H, OH), 10.19 (s, 1H, =N−NH), 8.28 (s, 1H, NH), 3.03 (d, J = 4.6 Hz, 3H, CH_3), 2.09 (s, 3H, (CH_3)CNOH), 2.03 ppm (s, 3H, (CH_3)CNNH). $^{13}C\{^1H\}$ NMR (101 MHz, DMSO-d_6,): δ 179.1, 155.1, 147.5, 31.6, 12.1, 9.9 ppm.

2.2.2 | 3-(Hydroxyimino)butan-2-ylidene-*N*,*N*-dimethylhydrazine-1-carbothioamide ($\mathbf{H_2L^{Me,Me}}$)

Colorless crystals (1.20 g, 74% yield). Anal. calcd for $C_7H_{14}N_4OS$ (202.09): C, 41.57; H, 6.98; N, 27.70; S, 15.85%. Found: C, 41.62; H, 7.17; N, 27.78; S, 15.97%. FT-IR (ATR): $\bar{\nu}$ 3300 (O–H), 3254, 3180

(N–H), 1596 (C=N)$_{tsc}$, 1538 (C=N)$_{ox}$, 1358 δ(O–H), 1014 (N–O), 829 cm^{-1} (C=S). UV–Vis: λ_{max} (ε_{max}) 297 nm (50,600 M^{-1} cm^{-1}). ^{1}H NMR (400 MHz, DMSO-d_6): δ 11.50 (s, 1H, OH), 9.46 (s, 1H, =N–NH), 3.26 (s, 6H, N (CH_3)$_2$), 2.08 (s, 3H, (CH_3)CNOH), 1.97 ppm (s, 3H, (CH_3)CNNH). ^{13}C{^{1}H} NMR (101 MHz, DMSO-d_6,): δ 181.4, 177.8, 154.8, 148.6 ppm.

2.2.3 | 3-(Hydroxyimino)butan-2-ylidene)-*N*-phenylhydrazine-1-carbothioamide (H_2L^{Ph})

Colorless crystals (1.66 g, 86% yield). Anal. calcd for $C_{11}H_{14}N_4OS$ (250.09): C, 52.78; H, 5.64; N, 22.38; S, 12.81%. Found: C 52.86; H, 5.70; N, 22.49; S, 12.89%. FT-IR (ATR): $\overline{\nu}$ 3320 (O–H), 3262, 3159 (N–H), 1590 (C=N)$_{tsc}$, 1538 (C=N)$_{ox}$, 1358 δ(O–H), 1010 (N–O), 829 cm^{-1} (C=S). UV–Vis: λ_{max} (ε_{max}): 303 nm (47,600 M^{-1} cm^{-1}). ^{1}H NMR (400 MHz, DMSO-d_6): δ 11.65 (s, 1H, OH), 10.60 (s, 1H, =N–NH), 9.89 (s, 1H, NH), 7.59 (d, J = 7.7 Hz, Ph), 2H, 7.37 (t, J = 7.6 Hz, 2H, Ph), 2.21 (t, J = 7.4 Hz, 1H, Ph), 2.18 (s, 3H, (CH_3)CNOH), 2.09 ppm (s, 3H, (CH_3)CNNH). ^{13}C{^{1}H} NMR (101 MHz, DMSO-d_6): δ 177.4, 155.1, 148.8, 139.5, 128.6, 125.9, 12.5, 9.9 ppm.

2.3 | Synthesis of Monometallic Pd^L Complexes

A mixture of *trans*-[$PdCl_2(MeCN)_2$] (206 mg, 1.0 mmol) and a TSC ligand precursor (1.0 mmol) in acetonitrile (10 mL) was stirred at room temperature for 1 h. 4-Aminopyridine (94 mg, 1.0 mmol) and Et_3N (140 μL, 0.59 mmol) were then added, and the reaction mixture was stirred for 12 h at room temperature. The precipitate was filtered off with suction, washed with acetonitrile, and dried under reduced pressure.

2.3.1 | [Pd(*N,N,S*-TSC^{Me})(4-NH_2Py)] (Mono-Pd^{Me})

Orange microcrystalline powder (282 mg, 73% yield). Anal. calcd for $C_{11}H_{16}N_6OPdS$ (386.01): C, 34.16; H, 4.17; N, 21.73; S, 8.29%. Found: C, 34.38; H, 4.35; N, 21.98; S, 8.48%. FT-IR (ATR): $\overline{\nu}$ 3319, 3202 (N–H), 1642 (C=N)$_{tsc}$, 1511 (C=N)$_{ox}$, 1134 (N–O), 728 (C–S), 338 cm^{-1} (Pd–S). UV–Vis: λ_{max} (ε_{max}) 257 (41400), 305 (31700), 398 (12400), 489 nm (4600 M^{-1} cm^{-1}). ^{1}H NMR (400 MHz, DMSO-d_6): δ 8.00 (d, J = 6.7 Hz, 2H, Ar), 7.12 (s, 1H, NH), 7.78 (s, 2H, NH_2), 6.50 (d, J = 4.7 Hz, 2H, Ar), 2.75 (d, J = 4.0 Hz, 3H, NCH_3), 2.14 (s, 3H, (CH_3)CNO), 1.82 ppm (s, 3H, (CH_3)CNN). ^{13}C{^{1}H} NMR (101 MHz, DMSO-d_6): δ 156.3, 151.6, 150.1, 109.7, 32.6, 13.6, 12.2 ppm.

2.3.2 | [Pd(*N,N,S*-TSC^{Me,Me})(4-NH_2Py)] (Mono-Pd^{Me,Me})

Orange-brown microcrystalline powder (280 mg, 70% yield). Anal. calcd for $C_{12}H_{18}N_6OPdS$ (400.03): C, 35.96; H, 4.53; N, 20.97; S, 8.00%. Found: C, 36.21; H, 4.75; N, 21.18; S, 8.28%. FT-IR (ATR): $\overline{\nu}$ 3327, 3198 (N–H), 1651 (C=N)$_{tsc}$, 1616 (C=N)$_{ox}$, 1132 (N–O), 728 (C–S), 335 cm^{-1} (Pd–S). UV–Vis: λ_{max} (ε_{max}) 258 (45500), 315 (30000), 382 (10900), 530 nm (8600 M^{-1} cm^{-1}). ^{1}H NMR (400 MHz, DMSO-d_6): δ 8.03 (d, J = 6.9 Hz, 2H, Ar), 6.79 (s, 2H, NH_2), 6.50 (d, J = 6.9 Hz, 2H, Ar), 3.10 (s, 6H, N (CH_3)$_2$), 2.12 (s, 3H, (CH_3)CNO), 1.81 ppm (s, 3H, (CH_3)CNN). ^{13}C{^{1}H} NMR (101 MHz, DMSO-d_6): δ 171.1, 158.7, 156.4, 151.5, 150.1, 109.7, 41.2, 13.5, 12.0 ppm.

2.3.3 | [Pd(*N,N,S*-TSC^{Ph})(4-NH_2Py)] (Mono-Pd^{Ph})

Red microcrystalline powder (399 mg, 89% yield). Anal. calcd for $C_{16}H_{18}N_6OPdS$ (448.03): C, 42.82; H, 4.04; N, 18.72; S, 7.14%. Found: C, 43.12; H, 4.26; N, 18.96; S, 7.31%. FT-IR (ATR): $\overline{\nu}$ 3302, 3194 (N–H), 1635 (C=N)$_{tsc}$, 1596 (C=N)$_{ox}$, 1084 (N–O), 748 (C–S), 337 cm^{-1} (Pd–S). UV–Vis: λ_{max} (ε_{max}) 258 (52800), 323 (34900), 382 (11200), 499 nm (8100 M^{-1} cm^{-1}). ^{1}H NMR (400 MHz, DMSO-d_6): δ 9.44 (s, 1H, NH), 8.01 (d, J = 6.9 Hz, 2H, Ph_{amine}), 7.62 (d, J = 7.8 Hz, 2H, Ph), 7.28 (t, J = 7.8 Hz, 2H, Ph), 6.95 (t, J = 7.3 Hz, 1H, Ph), 6.82 (s, 2H, NH_2), 6.53 (d, J = 6.9 Hz, 2H, Ph_{amine}), 2.27 (s, 3H, (CH_3)CNO), 1.86 ppm (s, 3H, (CH_3)CNN). ^{13}C{^{1}H} NMR (101 MHz, DMSO-d_6): δ 165.1, 163.0, 156.4, 151.6, 150.3, 141.8, 129.0, 122.2, 119.2, 109.8, 14.3, 12.0 ppm.

2.4 | Synthesis of Heterobimetallic Ru-Pd^L Complexes

A mixture of the [$RuCl_2$(*p*-cymene)]$_2$ dimer (200 mg, 0.327 mmol) and a Pd^L complex (**mono-Pd^{Me}**, **mono-Pd^{Me,Me}**, or **mono-Pd^{Ph}**) (0.654 mmol) in dichloromethane (10 mL) was stirred for 24 h at room temperature. The resulting precipitate was filtered, washed with dichloromethane, and dried under vacuum.

2.4.1 | [{$RuCl_2$(*p*-cymene)}-μ-(4-NH_2Py){Pd (TSC^{Me})}] (Ru-Pd^{Me})

Orange microcrystalline powder (160 mg, 71% yield). Anal. calcd for $C_{21}H_{30}Cl_2N_6OPdRuS$ (691.97): C, 36.40; H, 4.36; N, 12.13; 14.59; S, 4.63%. Found: C, 36.61; H, 4.53; N, 12.36; 14.72; S, 4.78%. FT-IR (ATR): $\overline{\nu}$ 3317, 3179 (N–H), 1616 (C=N)$_{tsc}$, 1511 (C=N)$_{ox}$, 1123 (N–O), 693 (C–S), 278 (Ru–Cl), 355 cm^{-1} (Pd–S). UV–Vis: λ_{max} (ε_{max}) 257 (61700), 312 (38800), 357 (14600), 467 nm (9600 M^{-1} cm^{-1}). ^{1}H NMR (400 MHz, DMSO-d_6): δ 7.98 (d, J = 5.6 Hz, 2H, Py_{Ar}), 7.12 (s, 1H, NH), 6.78 (s, 2H, NH_2), 6.49 (d, J = 5.7 Hz, 2H, Py_{Ar}), 5.82 (dd, J = 5.5 Hz, 4H, *p*-cym CH_{ar}), 2.83 (sept, J = 6.9 Hz, 1H, C*H* (CH_3)$_2$), *p*-cym), 2.76 (d, J = 4.0 Hz, 3H, NCH_3), 2.14 (s, 3H, (CH_3)CNO), 2.09 (s, 3H, CH_3, *p*-cym), 1.82 (s, 3H, (CH_3)CNN), 1.30 ppm (d, J = 6.7 Hz, 6H, CH (C*H*$_3$)$_2$, *p*-cym). ^{13}C{^{1}H} NMR (101 MHz, DMSO-d_6,): δ 156.3, 151.6, 150.1, 109.7, 106.9, 100.6, 86.8, 86.0, 32.6, 30.5, 22.0, 18.3, 13.6, 12.0 ppm.

2.4.2 | [{$RuCl_2$(*p*-cymene)}-μ-(4-NH_2Py){Pd (TSC^{Me,Me})}] (Ru-Pd^{Me,Me})

Orange microcrystalline powder (159 mg, 69% yield). Anal. calcd for $C_{22}H_{32}Cl_2N_6OPdRuS$ (706.03): C, 37.38; H, 4.56; N, 11.89; S, 4.53%. Found: C, 37.44; H, 4.69; N, 12.12; S, 4.77%. FT-IR (ATR): $\overline{\nu}$ 3324, 3198 (N–H), 1649 (C=N)$_{tsc}$, 1609 (C=N)$_{ox}$, 1210 (N–O), 713 (C–S), 268 (Ru–Cl), 364 cm^{-1} (Pd–S). UV–Vis: λ_{max} (ε_{max}) 256 (47800), 317 (24000), 360 (10800), 512 nm (8300 M^{-1} cm^{-1}). ^{1}H NMR (400 MHz, DMSO-d_6): δ 8.10 (d, J = 7.2 Hz, 2H, Py_{Ar} and 2H, NH_2), 6.80 (d, J = 7.1 Hz, 2H, Py_{Ar}), 5.83 (dd, J = 6.3 Hz, 4H, *p*-cym CH_{ar}), 3.18 (s, 6H, N (CH_3)$_2$ and 3H (CH_3)CNO), 2.83

(sept, $J = 6.9$ Hz, 1H, C*H* $(CH_3)_2$), *p*-cym), 2.09 (s, 3H, CH_3, *p*-cym), 2.07 (s, 3H, (CH_3)CNN), 1.20 ppm (d, $J = 6.8$ Hz, 6H, CH $(CH_3)_2$, *p*-cym). $^{13}C\{^1H\}$ NMR (101 MHz, DMSO-d_6): δ 179.2, 165.2, 160.3, 152.4, 140.3, 109.2, 106.8, 100.6, 86.8, 86.0, 40.0, 30.4, 22.0, 18.3, 14.4, 13.7 ppm.

2.4.3 | [{$RuCl_2$(*p*-cymene)}-μ-(4-NH_2Py){Pd (TSC^{Ph})}] (Ru-Pd^{Ph})

Red microcrystalline powder (207 mg, 84% yield). Anal. calcd for $C_{26}H_{32}Cl_2N_6OPdRuS$ (753.98): C, 41.36; H, 4.27; N, 11.13; S, 4.25%. Found: C, 41.55; H, 4.40; N, 11.31; S, 4.41%. FT-IR (ATR): $\overline{\nu}$ 3298, 3199 (N–H), 1636 $(C{=}N)_{tsc}$, 1509 $(C{=}N)_{ox}$, 1084 (N–O), 745 (C–S), 272 (Ru–Cl), 368 cm^{-1} (Pd–S). UV–Vis: λ_{max} (ε_{max}) 258 (47800), 316 (24000), 352 (10800), 512 nm (8300 $M^{-1}cm^{-1}$). ^1H NMR (400 MHz, DMSO-d_6): δ 9.44 (s, 1H, NH), 8.00 (d, $J = 6.8$ Hz, 2H, Py_{Ar}), 7.61 (d, $J = 7.9$ Hz, 2H, Ph), 7.28 (t, $J = 7.8$ Hz, 2H, Ph), 6.80 (t, $J = 7.2$ Hz, 1H, Ph), 6.83 (s, 2H, NH_2), 6.53 (d, $J = 6.9$ Hz, 2H, Py_{Ar}), 5.82 (dd, $J = 6.3$ Hz, 4H, *p*-cym CH_{ar}), 2.83 (sept, $J = 6.9$ Hz, 1H, C*H* $(CH_3)_2$), *p*-cym), 2.27 (s, 3H, (CH_3)CNOH), 2.09 (s, 3H, CH_3, *p*-cym), 1.85 (s, 3H, (CH_3)CNN), 1.20 ppm (d, $J = 6.9$ Hz, 6H, C*H* $(CH_3)_2$, *p*-cym). $^{13}C\{^1H\}$ NMR (101 MHz, DMSO-d_6): δ 165.1, 163.0, 156.4, 151.6, 150.3, 141.7, 129.0, 122.2, 119.2, 109.5, 106.8, 100.6, 86.8, 86.0, 30.4, 22.0, 18.3, 14.3, 12.0 ppm.

2.5 | X-Ray Crystallography

Crystal data were collected on a STOE IPDS 2T diffractometer at 200 K using the Mo-Kα radiation ($\lambda = 0.71073$ Å). Standard procedures were applied for data reduction [23]. The structure was solved by direct methods using SHELXS97 [24] and refined by using SHELXL2016 [25] programs included in the OLEX2 program package [26]. All nonhydrogen atoms were anisotropically refined, and the hydrogen atom positions were calculated with the "riding model" option of the SHELXL2016 program [25]. The molecular structure of **mono-Pd^{Me}** was represented using the ORTEP3 program (version 2014.1) and Mercury (version 4.3.1) [27, 28].

2.5.1 | Crystal Data for [Pd(*N,N,S*-TSC^{Me})(4-NH_2Py)] (Mono-Pd^{Me})

Yellowish-orange plates obtained by slow evaporation of a dichloromethane/methanol solution at room temperature, MF = $C_{11}H_{16}N_6OPdS$, MW = 386.76, monoclinic, $P2_1/a$, $a = 15.1417$ (13), $b = 6.3172$ (4), $c = 16.6878$ (15) Å, $\beta = 116.772$ (7)°, $V = 1425.1$ (2) $Å^3$, $Z = 4$, $\mu = 1.454$ mm^{-1}, reflections collected/unique = 13,048/3837 ($R_{int} = 0.0632$), final refinement converged with $R_1 = 0.0598$ and $wR_2 = 0.0611$ for all reflections, $GOF = 0.846$, $\Delta\rho_{max}/\Delta\rho_{min} = 0.60/-0.64$ e·$Å^{-3}$.

2.6 | Computational Studies

Structures of the compounds under investigation were optimized and their vibrational frequencies were calculated at the density functional theory (DFT) level using the hybrid functional M06 implemented in the Gaussian 09 software and DGDZVP basis set [29–31]. The influence of the solvent (DMSO) was evaluated in all calculations using the IEFPCM model [32]. The theoretical absorption spectra of the three Ru-Pd^L complexes were derived from TD-DFT calculations using the combination between the hybrid functional PBE0 [33, 34] and the same basis set used in the optimization, with DMSO as solvent. These calculations were performed for the first 200 excited states. The frontier molecular orbitals and those involved in the main transitions were rendered using the GaussView software.

2.7 | Reductive Heck Reactions

An oven-dried round-bottom flask was loaded with a monometallic Pd^L or a bimetallic Ru-Pd^L complex (0.055 mmol) and DMSO (3 mL) under a nitrogen atmosphere at room temperature. After stirring, an aryl halide (20.9 mmol), NBD (6.4 mL, 62.7 mmol), HCOOH (0.23 mL, 6 mmol), and Et_3N (1.00 mL, 7.5 mmol) were added, and the reaction mixture was heated to the desired temperature and stirred for 8 h under nitrogen (see Table 3). It was cooled to room temperature, diluted with EtOAc (20 mL), and washed with diluted HCl (30 mL) and water (30 mL). The organic layer was dried over anhydrous $MgSO_4$ and the solvent was evaporated under reduced pressure. The residue was subjected to column chromatography on silica gel using a 3/7 v/v ethyl acetate/hexane mixture to afford pure 5-phenylnorbornene. The product was characterized by ^1H NMR analysis. Analytic data matched those reported in the literature [35].

2.8 | ROMP Reactions

In a typical ROMP experiment, the **mono-Ru** (2.4 μmol) or a Ru-Pd^L complex (1.1 μmol) was dissolved in $CHCl_3$ (2 mL) with NBE (7.2 mmol, 0.68 g for mono-Ru; 3.3 mmol, 0.31 g for Ru-Pd^L) or Ph-NBE (7.2 mmol, 1.12 g for mono-Ru; variable amount for Ru-Pd^L), followed by the addition of ethyl diazoacetate (EDA). The reaction mixture was stirred for 30 min at 25°C, 50°C, or 90°C in a silicon oil bath (see Table 4). At room temperature, methanol (10 mL) was added, and the precipitated polymer was filtered, washed with methanol, and dried in a vacuum oven at 40°C until constant weight. The reported yields are the arithmetic average values from at least three catalytic runs.

2.9 | Reductive Heck/ROMP Reactions

An oven-dried round-bottom flask placed under a nitrogen atmosphere at room temperature was loaded with a Ru-Pd^L complex (0.055 mmol) and DMSO (3 mL). After stirring, iodobenzene (2.33 mL, 20.9 mmol), NBD (6.4 mL, 62.7 mmol), HCOOH (0.23 mL, 6 mmol), and Et_3N (1.00 mL, 7.5 mmol) were added. The reaction mixture was heated in an oil bath at 120°C for 8 h. It was then cooled to 50°C, and EDA (300 μL, 42.6 mmol) was added with a syringe under a nitrogen atmosphere. The reaction was continued for 30 more minutes. Methanol (10 mL) was added, and the precipitated polymer was filtered and dried under vacuum. Poly (Ph-NBE) was characterized by ^1H NMR analysis. Analytic data matched those reported in the literature [36].

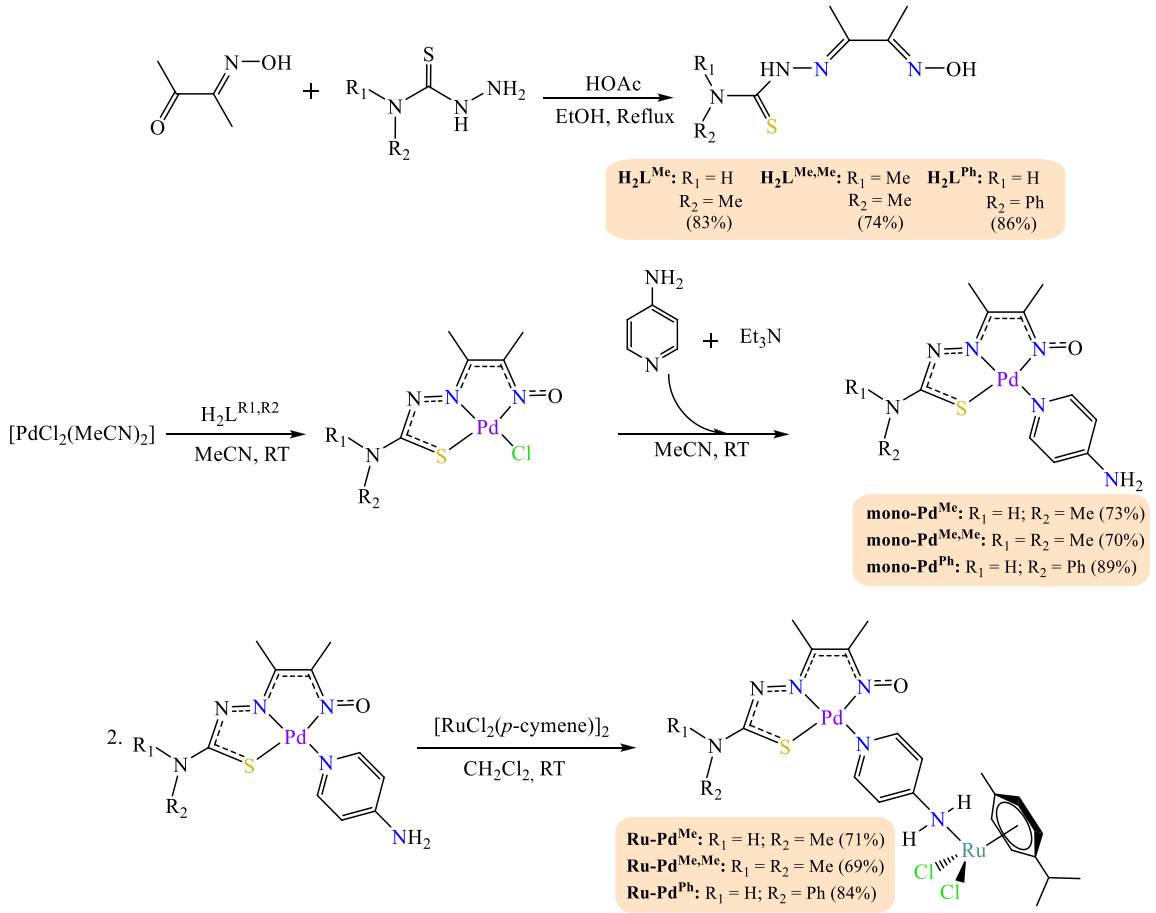

SCHEME 1 | Synthesis of H_2L thiosemicarbazide ligand precursors, monometallic Pd^L, and heterobimetallic Ru-Pd^L complexes.

3 | Results and Discussion

3.1 | Synthesis and Characterization

The ligand precursors $\mathbf{H_2L^{Me}}$, $\mathbf{H_2L^{Me,Me}}$, and $\mathbf{H_2L^{Ph}}$ were readily prepared by condensing diacetyl monoxime with three commercially available thiosemicarbazide derivatives in the presence of a catalytic amount of acetic acid in refluxing ethanol (Scheme 1). They were further reacted with $[PdCl_2(MeCN)_2]$ and 4-aminopyridine in 1:1:1 M proportions in the presence of triethylamine to afford the monometallic [Pd(*N,N,S*-TSC^{Me})(4-NH_2Py)] (**mono-Pd^{Me}**), [Pd(*N,N,S*-$TSC^{Me,Me}$)(4-NH_2Py)] (**mono-$Pd^{Me,Me}$**) and [Pd(*N,N,S*-TSC^{Ph})(4-NH_2Py)] (**mono-Pd^{Ph}**) complexes. Next, the amine function of the 4-NH_2Py ligand induced the cleavage of the $[RuCl_2(\eta^6\text{-}p\text{-cymene})]_2$ dimer to form the corresponding heterobimetallic [{$RuCl_2$(*p*-cymene)}-μ-(4-NH_2Py){Pd (TSC)}] complexes (**Ru-Pd^{Me}**, **Ru-$Pd^{Me,Me}$**, or **Ru-Pd^{Ph}**) in good yields (69%–84%) (Scheme 1). All the mono-Pd^L and Ru-Pd^L complexes were characterized by ^{1}H and ^{13}C NMR, FT-IR, and UV–Vis spectroscopies, elemental analysis, and cyclic voltammetry. Moreover, the molecular structure of the **mono-Pd^{Me}** complex was determined by single-crystal X-ray diffraction (XRD) analysis.

For the sake of comparison, we also prepared the $[RuCl_2$(*p*-cymene)$(PhNH_2)]$ complex (**mono-Ru**) by reacting the $[RuCl_2(\eta^6\text{-}p\text{-cymene})]_2$ dimer with aniline according to a previously published procedure [37]. Several attempts to synthesize the analogous $[RuCl_2$(*p*-cymene)(4-NH_2Py)] species (**mono-Ru***), which would have been a closer analogue of the ruthenium moiety present in our heterobimetallic complexes, remained unsuccessful. ^{1}H NMR spectra of the crude products recorded in CD_2Cl_2 revealed the presence of dimeric species, attributed to the coordination of the primary amine and pyridine to different ruthenium centers.

3.2 | Structural Analysis

The FT-IR spectra of the H_2L ligand precursors exhibited a low-intensity band around 3300–3353 cm^{-1} assigned to their O–H stretching vibration (Figure S1). The absence of this band in the mono-Pd^L complexes confirmed that a deprotonation had taken place upon complexation, leading to significant electronic delocalization (Figure S2). The FT-IR spectra of the mono-Pd^L and Ru-Pd^L complexes displayed bands around 1640 and 1600 cm^{-1} that were assigned to the stretching vibrations of the C=N (NH) and C=N (OH) bonds (Figures S2 and S3). In comparison with the free H_2L ligands, these bands were shifted by about 80 cm^{-1} to higher wavenumbers, in line with a coordination of the thiosemicarbazide ligands through their imine and oxime nitrogen atoms. In the heterobimetallic Ru-Pd^L complexes, the stretching vibration bands of the Ru–Cl and Pd–S bonds were located at *ca.* 270 and 360 cm^{-1}, respectively, which supports the presence of the two distinct metal centers in these dinuclear compounds.

The ^{1}H NMR spectra of the H_2L ligand precursors, mono-Pd^L, and Ru-Pd^L complexes were recorded in DMSO-d_6 at 298 K (Figures S4–S12). For the $\mathbf{H_2L^{Me}}$ and $\mathbf{H_2L^{Ph}}$ species, three singlets assigned to the hydrogen atoms of one OH and two NH groups were observed between 8 and 12 ppm. Contrastingly, the $\mathbf{H_2L^{Me,Me}}$ ligand exhibited only two signals in the same region due to the lack of a proton on its –NMe_2 group. Upon deprotonation and coordination to the palladium metal center, all these low field resonances disappeared, in agreement with the results of the FT-IR analyses showing the deprotonation and the complexation of the thiosemicarbazides. In the mono-Pd^L complexes, two doublets at *ca*. 8.00 and 6.50 ppm with a common $^3J_{H,H}$ coupling constant of 7 Hz were assigned to the aromatic protons of 4-aminopyridine, whose remote NH_2 group led to a singlet around 6.80 ppm. ^{1}H NMR spectra of the heterobimetallic Ru-Pd^L complexes featured all the resonances previously identified in the corresponding Ru and Pd monometallic complexes. In particular, the *p*-cymene ligand in the bimetallic complexes gave rise to a singlet and a doublet at *ca*. 2.10 and 1.20 ppm, respectively, for the CH_3Ar and $(CH_3)_2$CH methyl groups. In addition, the methine proton of the isopropyl substituent resonated as a septet at 2.83 ppm, and the aromatic hydrogen atoms gave a second-order multiplet at 6.50 ppm. On $^{13}C\{^1H\}$ NMR spectroscopy, all the resonances expected for the TSC ligands, mono-Pd^L, and Ru-Pd^L complexes were present, although we did not attempt to assign them precisely (Figures S13–S21).

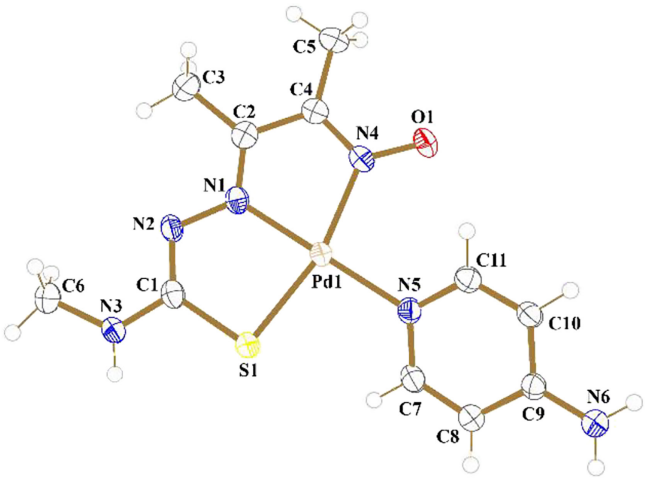

FIGURE 1 | Molecular structure of **mono-Pd^{Me}** with thermal ellipsoids drawn at the 50% probability level.

The molecular structure of **mono-Pd^{Me}** was determined by single-crystal XRD analysis (Figure 1, see also Figure S22). The complex crystallized in the monoclinic $P2_1/a$ space group. As expected, the metal center lay in a distorted square plane with a deviation of approximately 16° from the ideal geometry for the N4–Pd1–S1 angle (Table 1). The TSC ligand was coordinated in a *N,N,S*-tridentate, dianionic mode through the two nitrogen atoms of its azomethine and oxime groups, and its sulfur atom, forming two 5-membered chelate rings that presented a considerable delocalization of the π-electron density. Indeed, the distances measured for C1–S1, N1–N2, and C2–C4 displayed values intermediate between those typically associated with single and double bonds, as documented in the literature [38]. The Pd1–N1 and Pd1–N4 distances were similar, showing a reduction in the distortion of these bond lengths and making the TSC ligand almost planar. The N4–O1 bond length of 1.308 Å was consistent with the metrics observed in analogous Pd-TSC complexes, thereby supporting the deprotonation of the oxime group [39].

Computational studies were carried out on the mono-Pd^L and heterobimetallic Ru-Pd^L complexes to complement the

TABLE 1 | Selected bond lengths (Å) and angles (°) derived from XRD measurements and DFT calculations for mono-Pd^L complexes.

Bond length (Å)/angle (°)	Mono-Pd^{Me,Me}[a]	Mono-Pd^{Ph}[a]	Mono-Pd^{Me}[a]	Mono-Pd^{Me}[b]	Discrepancy theor./exp. (%)
Pd1 – N1	2.0111	2.0204	2.0185	1.968	1.65
Pd1 – N4	2.1085	2.1054	2.1055	2.053	2.56
Pd1 – S1	2.3835	2.3878	2.3904	2.282	4.77
Pd1 – N5	2.1221	2.1213	2.1231	2.056	3.26
N4 – O1	1.2679	1.2670	1.2673	1.308	3.11
C1 – S1	1.7849	1.7717	1.7806	1.772	0.50
N1 – N2	1.3653	1.3679	1.3687	1.395	1.89
C2 – C4	1.4523	1.4518	1.4522	1.462	0.67
N1 – Pd1 – N4	79.467	79.272	79.228	79.80	0.72
N1 – Pd1 – S1	82.169	82.521	82.285	84.47	2.59
N4 – Pd1 – S1	161.611	161.752	161.468	164.27	1.71
N4 – Pd1 – N5	99.389	99.615	99.480	100.24	1.23

[a]Calculated by DFT.
[b]Experimental values obtained by XRD analysis.

TABLE 2 | Selected bond lengths (Å) and angles (°) computed by DFT for the **Ru-Pd^{Me}**, **Ru-Pd^{Me,Me}**, **Ru-Pd^{Ph}**, **mono-Ru**, and **mono-Ru*** complexes.

Bond length (Å)/angle (°)	Ru-Pd^{Me}	Ru-Pd^{Me,Me}	Ru-Pd^{Ph}	mono-Ru	mono-Ru*
Ru1 – cnt[a]	1.7325	1.7300	1.7330	1.7312	1.7580
Ru1 – N6	2.2581	2.2579	2.2640	2.2290	2.2463
Ru1 – Cl1	2.4755	2.4653	2.4670	2.4810	2.4766
Ru1 – Cl2	2.4668	2.4751	2.4770	2.4681	2.4673
Pd1 – N1	2.0160	2.0109	2.0145	—	—
Pd1 – N4	2.1066	2.1090	2.1077	—	—
Pd1 – S1	2.3916	2.3844	2.3909	—	—
Pd1 – N5	2.1339	2.1338	2.1313	—	—
N4 – O1	1.2674	1.2682	1.2645	—	—
N6 – Ru – cnt[a]	128.606	127.289	128.439	128.400	129.875
Cl1 – Ru1 – Cl2	87.313	87.139	87.898	87.065	87.347
Cl1 – Ru1 – N6	82.149	82.150	89.938	82.409	82.238
Cl2 – Ru1 – N6	89.801	89.752	81.231	88.817	89.338
N1 – Pd1 – N5	178.904	178.796	178.469	—	—
N1 – Pd1 – S1	82.297	82.129	82.025	—	—
N4 – Pd1 – N5	99.766	99.700	100.002	—	—
S1 – Pd1 – N5	98.737	98.794	98.972	—	—

[a]cnt = centroid of the *p*-cymene six-membered ring.

structural characterization of these compounds. Selected bond lengths and angles calculated at the DFT level using the hybrid functional M06 and DGDZVP basis set [30, 31] are listed in Tables 1 and 2, while the optimized structures are shown in Figure 2. A minimum energy conformation was found for all the mono-Pd^{L} complexes. It featured a distorted square plane geometry with the TSC ligands coordinated to the metal center in a tridentate mode forming *N,N*- and *N,S*-five-membered chelate rings, and the 4-NH$_2$Py ligand *trans* to the azomethine nitrogen atom (Figure 2). Very gratifyingly, the discrepancies between theoretical and experimental bond lengths and angles for **mono-Pd^{Me}** did not exceed 5% (Table 1), which gave further credit to the geometries predicted for **mono-Pd^{Me,Me}** and **mono-Pd^{Ph}**. Only minimal changes in metrics were observed between these three complexes.

The optimal structures computed for Ru-Pd^{L} complexes exhibited a coordination environment around the Pd^{II} ion that closely resembled the one observed in mono-Pd^{L} complexes (Figure 2). Thus, the geometry around the Pd^{II} ion remained a distorted square plane, with only minor variations in bond lengths and angles. Although the bridging 4-NH$_2$Py ligand was the one most affected by the addition of a ruthenium-arene moiety, only a slight elongation of the Pd1 – N5 bond was observed when compared to the mono-Pd^{L} complexes (Table 2).

In order to better assess the impact of omitting the pyridinic nitrogen atom on the calculations and approximations associated with the **mono-Ru** complex derived from aniline, the [RuCl$_2$(*p*-cymene)(4-NH$_2$Py)] complex (**mono-Ru***) was also investigated by DFT. The bond lengths and angles computed for both compounds are listed in Table 2 while their optimized structures are displayed in Figure 3. In both cases, a minimum energy was reached for the typical "piano stool" geometry already observed in many analogous ruthenium-arene species [37, 40, 41]. Thus, the coordination environment around the Ru^{II} ion consisted of an η^6-(*p*-cymene), the amine, and two chlorido ligands, and the corresponding bond lengths (Ru1 – cnt, Ru1 – N6, Ru1 – Cl1, and Ru1 – Cl2) were similar up to 0.03 Å in the two complexes. In view of such a close resemblance, as predicted by theoretical calculations, the **mono-Ru** complex was considered a suitable model for the ruthenium moiety in the Ru-Pd^{L} complexes.

The electronic absorption spectra of the mono-Pd^{L} and Ru-Pd^{L} complexes (10^{-4} M solutions in DMSO) were recorded at 25°C (Figures S23–S28). They displayed high-energy bands at $\lambda \approx 255$–259 nm with extinction coefficients (ε) of 10^3 to 10^4 M^{-1} cm^{-1} and low-energy bands at $\lambda \approx 350$–530 nm with extinction coefficients of 10^3 M^{-1} cm^{-1}. The high-energy absorption bands were assigned to spin-allowed $n \rightarrow \pi^*$ transitions within the TSC ligands [42], while the low-energy absorption bands of the mono-Pd^{L} most likely originated from ligand-to-metal charge transfer (LMCT) transitions, as observed previously for other Pd-TSC complexes [43]. When more concentrated solutions were analyzed by UV–Vis spectroscopy, weak and broad bands with λ_{max} at *ca*. 476 or 513 nm and molar absorptivity of 1500 or 2300 M^{-1} cm^{-1} were detected for the mono-Pd^{L} and Ru-Pd^{L} complexes, respectively.

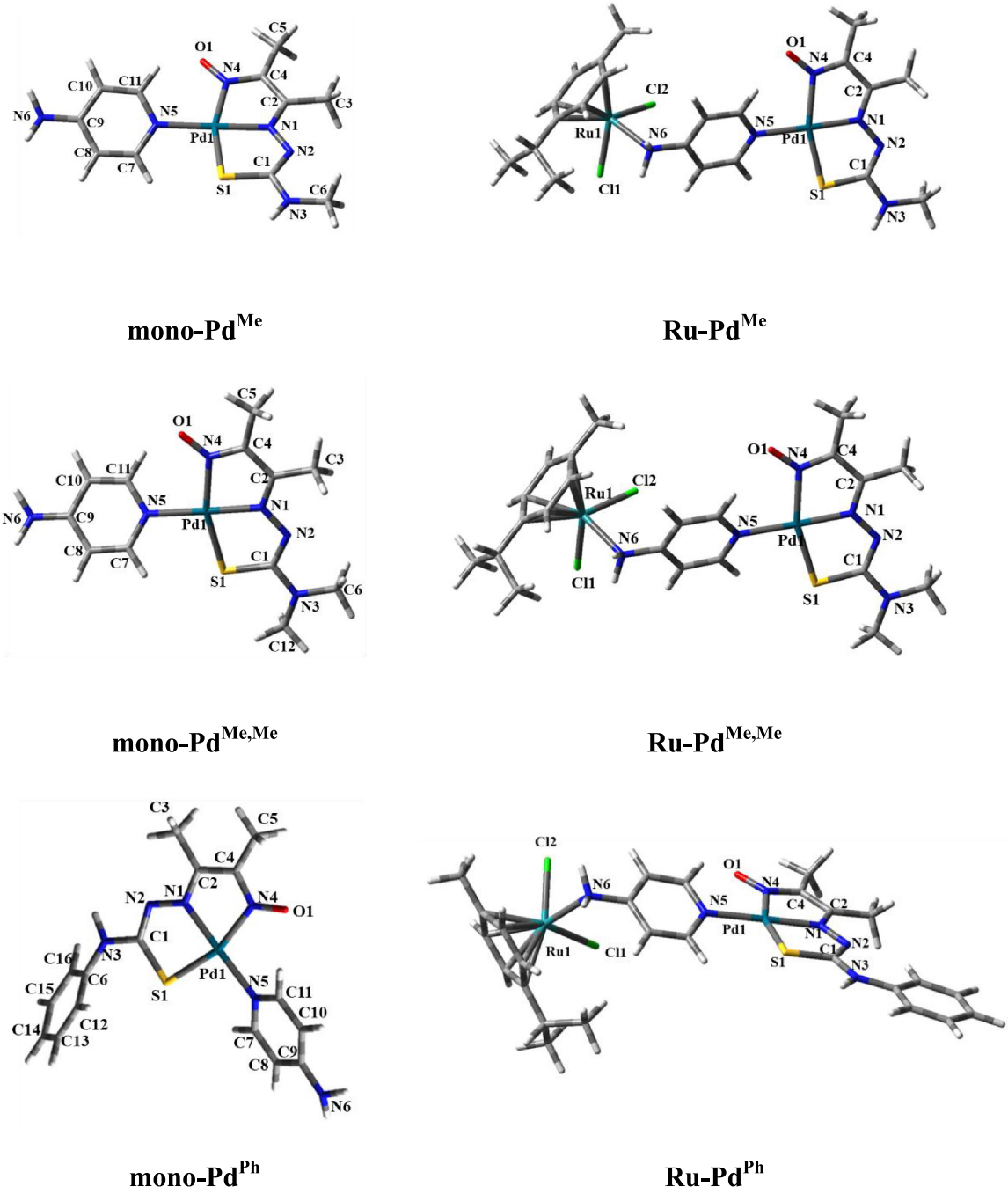

FIGURE 2 | DFT-optimized structures of mono-Pd^{L} and Ru-Pd^{L} complexes.

These bands probably arose from dπ (Pd) → π*(TSC) metal-to-ligand charge transfer (MLCT) transitions [44].

The theoretical absorption spectra of the three Ru-Pd^{L} complexes were derived from TD-DFT calculations with DMSO as solvent (Figures S26–S28). The calculated transitions agreed well with the experimental values of electronic absorption and the molecular orbitals associated with the transitions present in these heterobimetallic species. In particular, the good match between the theoretical and experimentally calculated oscillator strengths provided reliability to the analysis of the theoretically predicted structure (Figure 2). The TD-DFT calculations demonstrated that the intense bands observed below 370 nm resulted from intraligand transitions. In contrast, the bands above 370 nm were attributed to MLCT transitions, originating from the Pd or Ru center. Altogether, the spectral profiles of the three Ru-Pd^{L} complexes were very similar, suggesting that these species shared common geometrical features.

3.3 | Cyclic Voltammetry

The electrochemical behavior of the mono-Pd^{L}, Ru-Pd^{L}, and **mono-Ru** complexes was investigated by cyclic voltammetry vs. Ag/AgCl in DMSO containing 0.1 M tetrabutylammonium hexafluorophosphate (n-Bu_4NPF_6) as a supporting electrolyte with a scan rate of 50 mV s^{-1} at 25°C (Figure 4, see also Figures S29–S32). The oxidation potentials (E_{pa}) associated with the Pd$^{II/III}$

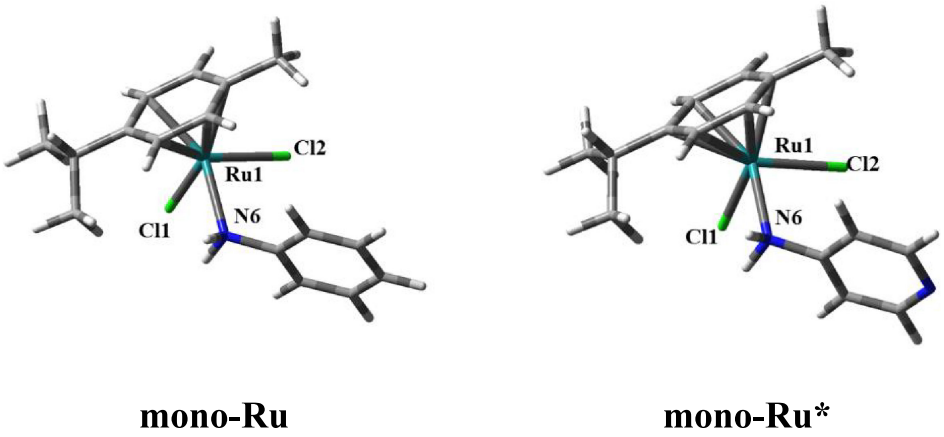

mono-Ru **mono-Ru***

FIGURE 3 | DFT-optimized structures of the **mono-Ru** and **mono-Ru*** complexes.

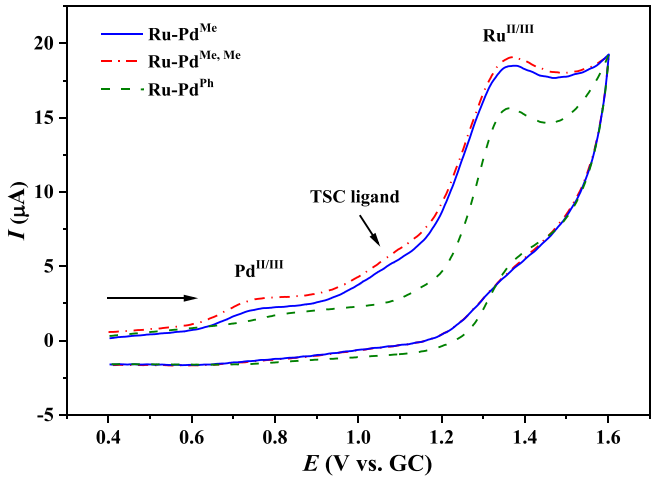

FIGURE 4 | Cyclic voltammograms of the **Ru-Pd^{Me}**, **Ru-Pd^{Me,Me}**, and **Ru-Pd^{Ph}** complexes in DMSO at 25 ± 0.1°C vs. glassy carbon at a scan rate of 50 mV s^{-1} ([Ru-Pd^{L}] = 1 mM, [*n*-Bu_4NPF_6] = 0.1 M).

conversion of the mono-Pd^{L} complexes strongly depended on the nature of their TSC ligand. Indeed, the E_{pa} value varied from 0.71 V for **mono-Pd^{Me,Me}** and 0.73 V for **mono-Pd^{Me}** to 0.89 V for **mono-Pd^{Ph}**, a 160 mV increase. All three mono-Pd^{L} complexes exhibited an additional wave at a more positive potential, which was attributed to the oxidation of the TSC ligand. The cyclic voltammograms for the Ru-Pd^{L} complexes revealed that the Pd$^{II/III}$ conversion underwent a cathodic shift of 40 mV for the **Ru-Pd^{Ph}** complex compared to **mono-Pd^{Ph}**. In contrast, the same palladium-centered redox process for the **Ru-Pd^{Me,Me}** and **Ru-Pd^{Ph}** complexes displayed an anodic shift with respect to the corresponding mono-Pd^{L} complexes.

In line with the observations made on mono-Pd^{L} complexes, an additional wave related to the TSC ligands was also detected around 1.0 V during the anodic scan of all Ru-Pd^{L} complexes. Furthermore, the anodic scan of the bimetallic complexes also revealed a new oxidation event attributed to the irreversible conversion of the Ru$^{II/III}$ pair at 1.37, 1.38, and 1.36 V for **Ru-Pd^{Me}**, **Ru-Pd^{Me,Me}** and **Ru-Pd^{Ph}**, respectively. In the Ru-Pd^{L} complexes, the oxidation processes centered on ruthenium exhibited a cathodic shift of *ca*. 90 mV relative to those observed in **mono-Ru** (Figure S32). The main electronic transitions predicted by theoretical calculations clearly demonstrated electronic communication between the Pd^{II} and Ru^{II} centers, mediated by the 4-NH_2Py ligand (Figure S33). Accordingly, the ruthenium center should be more electronically affected by the Pd-TSC moiety in the Ru-Pd^{L} complexes, which was confirmed by the greater displacement of the Ru$^{II/III}$ process compared to the Pd$^{II/III}$.

3.4 | Catalytic Tests

To investigate the hydroarylation of norbornadiene (NBD) via a reductive Heck reaction using the **mono-Pd^{Me}** complex, we varied the catalyst concentration (2 or 18 mM), the reaction temperature (60°C, 90°C, or 120°C), and the nature of the aryl halide (PhI or PhCl). In all these reactions, the HCOOH/Et_3N system was employed as a hydride source to favor reducing conditions [45, 46], and NBD was introduced in excess to minimize the likelihood of adding PhX to both its double bonds. A first run conducted in DMSO at 60°C with a [Pd]/[PhX]/[NBD] ratio of 1/380/1140 afforded a 35% conversion of NBD and a 23% yield of 5-phenylnorbornene (Ph-NBE) after purification by column chromatography (Table 3, Entry 1). The remaining NBD could be easily removed due to its volatility and did not interfere with the product isolation. Increasing the temperature to 90 and then to 120°C eventually afforded a quantitative conversion within 8 h (Table 3, Entries 2 and 3). Reducing the catalyst concentration from 18 to 2 mM significantly decreased the conversion and the yield to 28% and 26%, respectively (Table 3, Entry 4). As expected, the use of chlorobenzene instead of iodobenzene also impacted negatively the course of the reaction, as shown in Entry 5, Table 3. Higher turnover numbers (TON) were achieved when the catalyst concentration was maintained at 18 mM, and the [Pd]/[NBD]/[PhX] ratio was changed to 1/418/1344 (Table 3, Entry 6). The **mono-Pd^{Me,Me}** and **mono-Pd^{Ph}** complexes were also highly efficient catalysts for the hydroarylation of NBD under the experimental conditions optimized for **mono-Pd^{Me}** (Table 3, Entries 7 and 8). Contrastingly, the heterobimetallic Ru-Pd^{L} compounds displayed a lower activity compared to their monometallic counterparts (Table 3, Entries 9–14), although we were still able to achieve a 96% conversion with the **Ru-Pd^{Ph}** complex under optimized conditions (Table 3, Entry 12).

To probe the mechanism of the Heck reaction using our catalytic system, we monitored the reaction between the **mono-Pd^{Me}**

TABLE 3 | Reductive Heck reaction of NDB with an aryl halide using mono-Pd^{L} and Ru-Pd^{L} complexes as catalysts.[a]

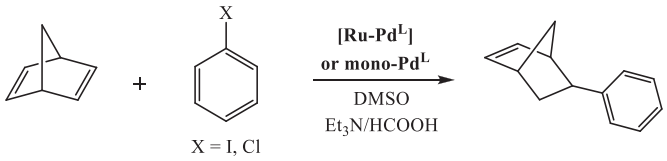

Entry	Cat.	Cat. Conc. (mM)	PhX	T (°C)	Conv. (%)[b]	Yield (%)[c]	TON
1	**Mono-Pd^{Me}**	18	PhI	60	35	23	30
2	**Mono-Pd^{Me}**	18	PhI	90	55	37	80
3	**Mono-Pd^{Me}**	18	PhI	120	100	96	200
4	**Mono-Pd^{Me}**	2	PhI	120	28	26	10
5	**Mono-Pd^{Me}**	18	PhCl	120	73	72	150
6[d]	**Mono-Pd^{Me}**	18	PhI	120	100	99	420
7	**Mono-Pd^{Me,Me}**	18	PhI	120	92	91	190
8	**Mono-Pd^{Ph}**	18	PhI	120	100	97	210
9	**Ru-Pd^{Me}**	18	PhI	120	87	86	180
10	**Ru-Pd^{Me}**	18	PhI	90	39	37	80
11	**Ru-Pd^{Me}**	2	PhI	90	44	41	10
12[d]	**Ru-Pd^{Me}**	18	PhI	120	98	96	400
13	**Ru-Pd^{Me,Me}**	18	PhI	120	93	92	190
14	**Ru-Pd^{Ph}**	18	PhI	120	95	93	190

[a]Experimental conditions: catalyst (0.055 mmol), NBD (20.9 mmol), PhX (67.2 mmol) in DMSO (3 mL) for 8 h.
[b]Determined by GC analysis using anisole as an internal standard.
[c]Yield of isolated product after purification by column chromatography.
[d]The [Pd]/[PhI]/[NBD] ratio was 1/418/1344.

complex and iodobenzene in DMSO-d_6. ^{1}H NMR spectroscopy showed the formation of a hexacoordinated [PdI(TSC)(4-NH$_2$Py)Ph] intermediate. Indeed, the aromatic protons of the aryl halide were shifted to higher field compared to the free substrate (Figure S34). Additionally, the resonances observed for the protons of TSC and 4-NH$_2$Py confirmed the coordination of these ligands to the metal center. Altogether, these observations suggest that the initial step of the reductive coupling mediated by the **mono-Pd^{Me}** complex involves the oxidative addition of PhI via an associative pathway. When norbornadiene was further added to the reaction mixture, we could not detect any free amine signals on ^{1}H NMR spectroscopy (Figure S35). This observation is crucial, as it suggests that following NBD coordination, the 4-NH$_2$Py ligand remains bound to the Pd center. This retention is essential to preserve the integrity of the Ru moiety within the Ru-Pd^{L} heterobimetallic species, ensuring that a single species is responsible for the tandem catalysis.

Next, the influence of a palladium center on ROMP reactions was evaluated using the **mono-Pd^{Me}** complex as a precatalyst. No polymer was isolated when norbornene (NBE) was mixed with this compound in chloroform at 50°C for 30 min ([NBE]/[**mono-Pd^{Me}**] = 3000) in the presence of ethyl diazoacetate ([EDA]/[mono-Pd^{Me}] = 50). This lack of reactivity is not surprising and indicates that the Pd-TSC moiety does not promote ROMP reactions. It should be pointed out that the addition of EDA is essential to achieve any ROMP activity when the catalyst precursor lacks an alkylidene moiety needed to initiate metathesis reactions. Accordingly, preliminary tests carried out with **mono-Ru** and Ru-Pd^{L} complexes confirmed that these species were equally inactive in the absence of a carbene source. Yet, the addition of EDA to these ruthenium precursors triggered the in situ formation of metathetically active Ru = CHR species and led to the polymerization of 5-phenylnorbornene (Ph-NBE) (Table 4). Reactions carried out at 25 and 50°C using molar ratios of [Ph-NBE]/[**Ru-Pd^{Me}**] = 3000 and [EDA]/[**Ru-Pd^{Me}**] = 107 for 30 min afforded low yields of poly (Ph-NBE) (Table 4, Entries 1 and 2). However, the catalytic activity of the **Ru-Pd^{Me}** complex increased with increasing V_{EDA} (up to [EDA]/[**Ru-Pd^{Me}**] = 321) (Table 4, Entries 2–4). An excessive amount of EDA ([EDA]/[Ru] ≥ 429) was, however, detrimental to the polymerization, possibly because it resulted in an uncontrolled coordination of EDA to the Ru center (Table 4, Entry 5). Varying the monomer-to-catalyst ratio was also investigated. Yields increased with increasing [Ph-NBE]/[Ru-Pd^{L}] molar ratio, from 1000, with yields < 20%, reaching 61% at a ratio of 3000. (Table 4, Entries 5–7). This ratio was used for all our subsequent experiments.

The ROMP of unsubstituted norbornene (NBE) mediated by the **Ru-Pd^{Me}** complex was carried out to probe the influence of the monomer 5-phenyl substituent on the outcome of the reaction. This test was performed with a [NBE]/[Ru-Pd^{L}] molar ratio = 3000 and [EDA]/[**Ru-Pd^{Me}**] molar ratio = 107 at 50°C for 30 min (Table 4, Entry 8). Under these conditions,

polynorbornene was isolated in 85% yield, a value close to the one obtained when Ph-NBE was employed (cf. Table 4, Entry 4). This result indicates that the presence of a distant phenyl group does not significantly reduce the catalyst activity. When norbornadiene was reacted under the same experimental conditions, the yield was 80% (Table 4, Entry 9). This result confirmed that the **Ru-Pd^{Me}** complex was equally active for the ROMP of NBE and NBD.

TABLE 4 | ROMP of Ph-NBE and NBE catalyzed by Ru-Pd^{L} or **mono-Ru** complexes upon activation with ethyl diazoacetate (EDA).[a]

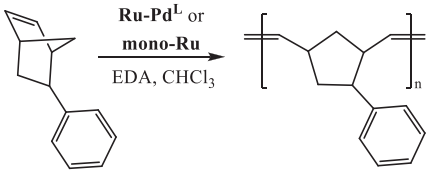

Entry	Cat.	Monomer	NBE/Ru	T (°C)	V_{EDA} (μL)	[EDA]/[Ru]	Yield (%)[b]
1	**Ru-Pd^{Me}**	Ph-NBE	3000	25	100	107	17
2	**Ru-Pd^{Me}**	Ph-NBE	3000	50	100	107	28
3	**Ru-Pd^{Me}**	Ph-NBE	3000	50	200	214	42
4	**Ru-Pd^{Me}**	Ph-NBE	3000	50	300	321	73
5	**Ru-Pd^{Me}**	Ph-NBE	3000	50	400	429	61
6	**Ru-Pd^{Me}**	Ph-NBE	1000	50	300	321	12
7	**Ru-Pd^{Me}**	Ph-NBE	2000	50	300	321	18
8	**Ru-Pd^{Me}**	NBE	3000	50	300	321	85
9	**Ru-Pd^{Me}**	NBD	3000	50	300	321	80
10	**Ru-Pd^{Me,Me}**	Ph-NBE	3000	50	300	321	81
11	**Ru-Pd^{Ph}**	Ph-NBE	3000	50	300	321	72
12	**Mono-Ru**	Ph-NBE	3000	50	300	147	81
13	**Mono-Ru**	NBE	3000	50	300	147	98

[a]Experimental conditions: catalyst (2.4 μmol of mono-Ru or 1.1 μmol of Ru-Pd^{L}), monomer, and EDA in $CHCl_3$ (2 mL) for 30 min.
[b]Yield of isolated polymer, average value from at least three catalytic runs.

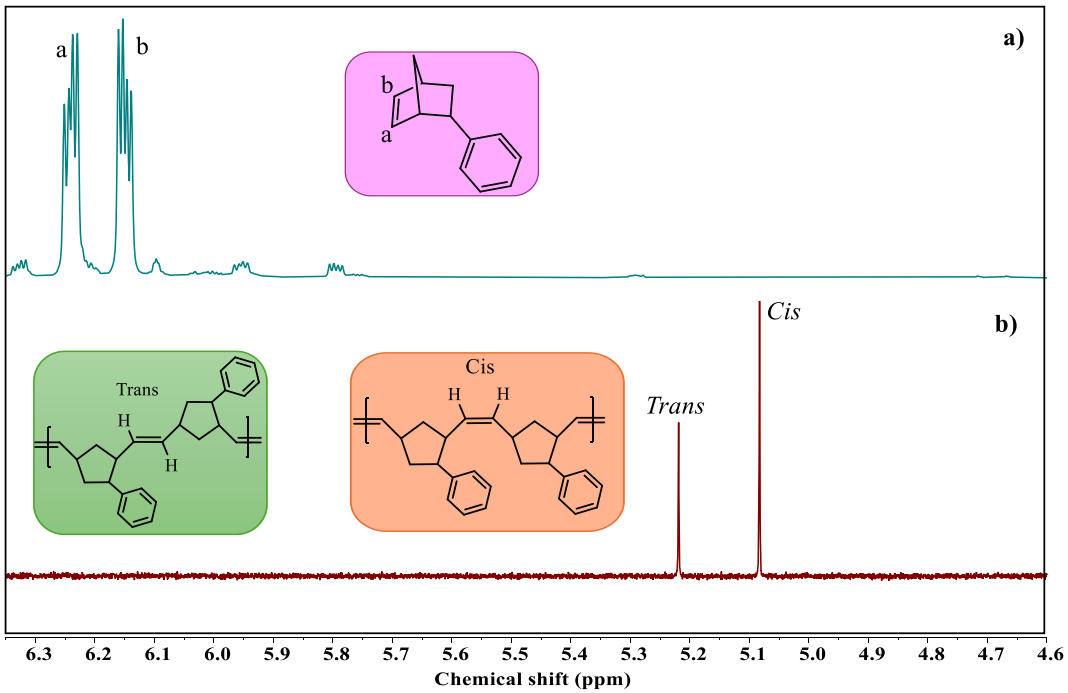

FIGURE 5 | ^{1}H NMR spectra in $CDCl_3$ of the olefinic protons of (a) Ph-NBE and (b) poly (Ph-NBE) obtained via tandem catalysis.

Comparing the yields obtained with the three Ru-Pd^{L} complexes in the ROMP of Ph-NBE showed that the **Ru-Pd^{Ph}** complex was the least active catalyst of the series (Table 4, Entries 4, 10, and 11), which can be explained by a lower accessibility of the Ru redox pair, as observed by cyclic voltammetry (cf. Figure 4). Performing the ROMP of Ph-NBE and NBE with the **mono-Ru** complex under the same experimental conditions that were used for the heterobimetallic Ru-Pd^{L} catalyst precursors led to slightly higher yields of polymers (Table 4, Entries 12 and 13). We hypothesize that the increased steric pressure exerted on ruthenium in the dinuclear species might hinder the approach of the olefin to the metal center.

Since the heterobimetallic Ru-Pd^{L} complexes demonstrated a good catalytic activity for the synthesis of 5-phenylnorbornene via the reductive Heck reaction of norbornadiene and iodobenzene, and for its ROMP in the presence of ethyl diazoacetate, the next step was to carry out both reactions in one pot, aiming for tandem catalysis. Because **Ru-Pd^{Me,Me}** showed the highest activity in the ROMP of Ph-NBE, this complex was selected for mediating the dual-catalytic process. The reductive Heck reaction was carried out with a [**Ru-Pd^{Me,Me}**]/[NBD]/[PhI] ratio of 1/418/1344 in DMSO at 120°C. After 8 h, the vessel was cooled to 50°C, and a carbene source was added ([EDA]/[Ru] = 321) to initiate the ROMP of Ph-NBE. After 30 min, the polymer was precipitated with methanol and dried under vacuum. It was isolated in 80% yield. The successful synthesis of the intermediate hydroarylation product was evidenced by ^{1}H NMR spectroscopy. Two resonances associated with the hydrogens of the bicyclic olefin were observed at 6.15 and 6.23 ppm (Figure 5a). Only a small portion of the final polymer could be dissolved in chloroform after several hours of stirring. An aliquot of this solution was filtered and used for ^{1}H NMR analysis, which showed the olefinic hydrogens of *cis*- and *trans*-poly (Ph-NBE) at 5.08 and 5.22 ppm, respectively (Figure 5b, see also Figure S36). These data confirmed the successful tandem polymerization to produce poly (Ph-NBE). The absence of olefinic signals characteristic of poly (NBD) [47] in the spectrum indicated that Ph-NBE was the monomer preferentially consumed in the ROMP reaction. Multiple attempts to dissolve the polymer obtained in THF were carried out. However, the quantity of materials solubilized was consistently insufficient to permit an accurate SEC analysis.

4 | Conclusion

In this study, we successfully synthesized and characterized a series of mono-Pd^{L} and heterobimetallic Ru-Pd^{L} complexes, revealing their structural and electronic features through various experimental and theoretical methods. The coordination modes of the thiosemicarbazide ligands in mono-Pd^{L} and Ru-Pd^{L} complexes were confirmed by FT-IR, multinuclear NMR, and X-ray diffraction analyses, whereas computational methods validated the geometric and electronic structures of the mono- and heterobimetallic assemblies, showing good agreement with the experimental data. Electrochemical studies of the three Ru-Pd^{L} complexes showed the presence of Ru$^{II/III}$ and Pd$^{II/III}$ redox pairs, with a shift compared with those from the monometallic species. The mono-Pd^{L} complexes efficiently catalyzed the reductive Heck reaction of norbornadiene and iodobenzene, achieving almost quantitative yields of 5-phenylnorbornene under optimized conditions. Furthermore, the Ru-Pd^{L} complexes were able to trigger separately the hydroarylation of NBD and the ROMP of Ph-NBE. Notably, **Ru-Pd^{Me,Me}** also functioned as an efficient dual catalyst, successfully mediating both reactions in a single process, thereby allowing the synthesis of poly (Ph-NBE) from NBD in one pot. Altogether, these findings provide valuable insights into the coordination chemistry and catalytic versatility of heterobimetallic complexes, highlighting their potentials in selective transformations, multimetal catalysis, and polymerization reactions.

Author Contributions

Thais R. Cruz: Writing – review and editing, writing – original draft, methodology, Investigation, formal analysis, data curation. **Juliana I. P. Maia:** methodology. **Pedro I. S. Maia:** formal analysis, writing – review and editing. **Antonio E. H. Machado:** formal analysis, writing – review and editing. **Beatriz E. Goi:** supervision, funding acquisition, conceptualization. **Lionel Delaude:** supervision, writing – review and editing, funding acquisition, conceptualization. **Valdemiro P. Carvalho-Jr:** supervision, writing – review and editing, funding acquisition, conceptualization.

Acknowledgements

This research was funded by the CNPq (grant 311747/2023-0), FAPEMIG (RED-00116-23) and FAPESP (grant 2021/13128-1 and Proc. 2021/11873-1). The authors acknowledge the financial support provided by PROPe/UNESP through the public call Edital 04/2024. The financial support of CNPq (Proc. 88881.690136/2022-01) is gratefully acknowledged (sandwich doctoral fellowship to TRC). The Article Processing Charge for the publication of this research was funded by the Coordenação de Aperfeiçoamento de Pessoal de Nível Superior - Brasil (CAPES) (ROR identifier: 00x0ma614).

Conflicts of Interest

The authors declare no conflicts of interest.

Data Availability Statement

Data that support the findings of this study are available in the supporting information of this article. CCDC 2422499 contains the crystallographic data for [Pd(*N,N,S*-TSC^{Me})(4-NH$_2$Py)] (**mono-Pd^{Me}**). These data can be obtained free of charge via www.ccdc.cam.ac.uk/data_request/cif, or by emailing data_request@ccdc.cam.ac.uk, or by contacting the Cambridge Crystallographic Data Centre, 12 Union Road, Cambridge CB2 1EZ, UK, fax: +441223 336033.

References

1. R. A. Sheldon, I. W. C. E. Arends, and U. Hanefeld, *Green Chemistry and Catalysis* (Wiley-VCH, 2007).

2. B. Cornils, W. A. Herrmann, H.-W. Zanthoff, and C.-H. Wong, *Catalysis from A to Z: A Concise Encyclopedia* (Wiley-VCH, 2013).

3. J. Hagen, *Industrial Catalysis: A Practical Approach* (Wiley-VCH, 2015).

4. D. Astruc, *Organometallic Chemistry and Catalysis* (Springer, 2007).

5. B. Cornils, W. A. Herrmann, M. Beller, and R. Paciello, *Applied Homogeneous Catalysis With Organometallic Compounds* (Wiley-VCH, 2017).

6. B. G. Cooper, J. W. Napoline, and C. M. Thomas, "Catalytic Applications of Early/Late Heterobimetallic Complexes," *Catalysis Reviews* 54 (2012): 1–40.

7. D. Das, S. S. Mohapatra, and S. Roy, "Recent Advances in Heterobimetallic Catalysis Across a "Transition Metal–Tin" Motif," *Chemical Society Reviews* 44 (2015): 3666–3690.

8. M. M. Lorion, K. Maindan, A. R. Kapdi, and L. Ackermann, "Heteromultimetallic Catalysis for Sustainable Organic Syntheses," *Chemical Society Reviews* 46 (2017): 7399–7420.

9. H.-C. Yu and N. P. Mankad, "Catalytic Reactions by Heterobimetallic Carbonyl Complexes With Polar Metal–Metal Interactions," *Synthesis* 53 (2021): 1409–1422.

10. P. C. Abhyankar and C. M. Thomas, "Hydrogenation Reactions With Heterobimetallic Complexes," *Angewandte Chemie, International Edition* 63 (2024): e202416100.

11. D. Balcells, E. Clot, and O. Eisenstein, "C-H Bond Activation in Transition Metal Species From a Computational Perspective," *Chemical Reviews* 110 (2010): 749–823.

12. J. Fu, X. Huo, B. Li, and W. Zhang, "Cooperative Bimetallic Catalysis in Asymmetric Allylic Substitution," *Organic & Biomolecular Chemistry* 15 (2017): 9747–9759.

13. E. L. Dias and R. H. Grubbs, "Synthesis and Investigation of Homo- and Heterobimetallic Ruthenium Olefin Metathesis Catalysts Exhibiting Increased Activities," *Organometallics* 17 (1998): 2758–2767.

14. H. K. Chaves, C. P. Ferraz, V. P. Carvalho, and B. S. Lima-Neto, "Tuning the Activity of Alternative Ru-Based Initiators for Ring-Opening Metathesis Polymerization of Norbornene and Norbornadiene by the Substituent in 4-CH2R-Piperidine," *Journal of Molecular Catalysis A: Chemical* 385 (2014): 46–53.

15. P. Borim, B. S. Lima-Neto, B. E. Goi, and V. P. Carvalho, "Ru-Dimethyl Sulfoxide Complexes as Catalysts Precursors for ROMP of Norbornene and ATRP of Methyl Methacrylate," *Inorganica Chimica Acta* 456 (2017): 171–178.

16. R. A. N. Silva, P. Borim, L. R. Fonseca, B. S. Lima-Neto, J. L. Silva Sá, and V. P. Carvalho-Jr, "Non-Carbene Complex $[RuCl_2(PPh_3)_2$(azocane)] as Active Catalyst Precursor for ROMP and ATRP," *Catalysis Letters* 147 (2017): 1144–1152.

17. M. B. A. Afonso, T. R. Cruz, Y. F. Silva, et al., "Ruthenium (II) Complexes of Schiff Base Derived From Cycloalkylamines as Pre-Catalysts for ROMP of Norbornene and ATRP of Methyl Methacrylate," *Journal of Organometallic Chemistry* 851 (2017): 225–234.

18. G. H. C. Masson, T. R. Cruz, P. D. S. Gois, et al., "Ruthenium–Nickel Heterobimetallic Complex as a Bifunctional Catalyst for ROMP of Norbornene and Ethylene Polymerization," *New Journal of Chemistry* 45 (2021): 11466–11473.

19. P. D. D. S. Gois, J. I. P. Maia, G. H. C. Masson, et al., "Monometallic and Heterobimetallic Ruthenium (II) and Palladium (II) Complexes Based on a Pyridine Hydrazone Ligand as Bifunctional Catalysts for ROMP of Norbornene and Ethylene Polymerization," *Applied Organometallic Chemistry* 36 (2021): e6491.

20. T. R. Cruz, G. H. C. Masson, K. A. E. Amorim, A. E. H. Machado, B. E. Goi, and V. P. Carvalho-Jr, "Ru/Pd Complex and Its Monometallic Fragments as Catalysts for Norbornene Polymerization via ROMP and Addition," *Catalysts* 12 (2022): 1111.

21. M. A. Andrews, T. C. T. Chang, C. F. Cheng, T. J. Emge, K. P. Kelly, and T. F. Koetzle, "Synthesis, Characterization, and Equilibria of Palladium (II) Nitrile, Alkene, and Heterometallic Cyclopentane Complexes Involved in Metal Nitro Catalyzed Alkene Oxidation Reactions," *Journal of the American Chemical Society* 106 (1984): 5913–5920.

22. A. C. R. Gonçalves, Z. A. Carneiro, C. G. Oliveira, et al., "Pt^{II}, Pd^{II} and Au^{III} Complexes With a Thiosemicarbazone Derived From Diacethylmonooxime: Structural Analysis, Trypanocidal Activity, Cytotoxicity and First Insight Into the Antiparasitic Mechanism of Action," *European Journal of Medicinal Chemistry* 141 (2017): 615–631.

23. Stoe & Cie "X-RED32; Stoe & Cie GmbH: Darmstadt, Germany" (2002).

24. G. M. Sheldrick, "A Short History of SHELX," *Acta Crystallographica Section A: Foundations of Crystallography* 64 (2008): 112–122.

25. G. M. Sheldrick, "Crystal Structure Refinement With SHELXL," *Acta Crystallographica Section C, Structural Chemistry* 71 (2015): 3–8.

26. O. V. Dolomanov, L. J. Bourhis, R. J. Gildea, J. A. Howard, and H. Puschmann, "OLEX2: A Complete Structure Solution, Refinement and Analysis Program," *Journal of Applied Crystallography* 42 (2009): 339–341.

27. L. J. Farrugia, "Win GX and ORTEP for Windows: An Update," *Journal of Applied Crystallography* 45 (2012): 849–854.

28. C. F. Macrae, I. Sovago, S. J. Cottrell, et al., "Mercury 4.0: From Visualization to Analysis, Design and Prediction," *Journal of Applied Crystallography* 53 (2020): 226–235.

29. N. Godbout, D. R. Salahub, J. Andzelm, and E. Wimmer, "Optimization of Gaussian-Type Basis Sets for Local Spin Density Functional Calculations. Part I. Boron Through Neon, Optimization Technique and Validation," *Canadian Journal of Chemistry* 70 (1992): 560–571.

30. Y. Zhao and D. G. Truhlar, "The M06 Suite of Density Functionals for Main Group Thermochemistry, Thermochemical Kinetics, Noncovalent Interactions, Excited States, and Transition Elements: Two New Functionals and Systematic Testing of Four M06-Class Functionals and 12 Other Functionals," *Theoretical Chemistry Accounts* 120 (2007): 215–241.

31. M. J. Frisch, G. W. Trucks, H. B. Schlegel, et al., *Gaussian 09, Revision E.01* (Gaussian Inc., 2013).

32. J. Tomasi, B. Mennucci, and E. Cancès, "The IEF Version of the PCM Solvation Method: An Overview of a New Method Addressed to Study Molecular Solutes at the QM Ab Initio Level," *Journal of Molecular Structure: THEOCHEM* 464 (1999): 211–226.

33. A. Carlo and V. Barone, "Toward Reliable Density Functional Methods Without Adjustable Parameters: The PBE0 Model," *Journal of Chemical Physics* 110 (1999): 6158–6170.

34. D. Coskun, S. V. Jerome, and R. A. Friesner, "Evaluation of the Performance of the B3LYP, PBE0, and M06 DFT Functionals, and DBLOC-Corrected Versions, in the Calculation of Redox Potentials and Spin Splittings for Transition Metal Containing Systems," *Journal of Chemical Theory and Computation* 12 (2016): 1121–1128.

35. A. N. Artemov, E. V. Sazonova, M. V. Revin, K. V. Rybkin, M. A. Lazarev, and V. I. Faerman, "[2+ 4] Cycloaddition of η^6-(Styrene) Chromium Tricarbonyl and Conjugated Dienes," *Russian Chemical Bulletin* 60 (2011): 2103–2106.

36. A. G. Barrett, B. T. Hopkins, A. C. Love, and L. Tedeschi, "Parallel Synthesis of Terminal Alkynes Using a ROMPgel-Supported Ethyl 1-Di azo-2-Oxopropylphosphonate," *Organic Letters* 6 (2004): 835–837.

37. C. Binnani, D. Tyagi, R. K. Rai, S. M. Mobin, and S. K. Singh, "C−H Bond Activation/Arylation Catalyzed by Arene–Ruthenium–Aniline Complexes in Water," *Chemistry, An Asian Journal* 11 (2016): 3022–3031.

38. W.-K. Li, G.-D. Zhou, and T. Mak, *Advanced Structural Inorganic Chemistry. IUCr Texts on Crystallography 10* (Oxford Science Publications, 2008).

39. K. V. Katti, P. R. Singh, and C. L. Barnes, "Transition-Metal Chemistry of Main-Group Hydrazides. Part 2. A New Oxime Thiosemicarbazide Framework as a Novel SN Multifunctional Tripodal Ligand for Palladium(II): Synthetic and X-Ray Crystal Structural Investigations," *Journal of the Chemical Society, Dalton Transactions* 14 (1993): 2153–2156.

40. T. R. Cruz, E. A. Silva, D. P. Oliveira, et al., "Dual Catalytic Performance of Arene-Ruthenium Amine Complexes for Norbornene Ring-Opening Metathesis and Methyl Methacrylate Atom-Transfer Radical Polymerizations," *Applied Organometallic Chemistry* 34 (2020): e5602.

41. D. P. Oliveira, T. R. Cruz, D. M. Martins, et al., "In Situ-Generated Arene-Ruthenium Catalysts Bearing Cycloalkylamines for the Ring-Opening Metathesis Polymerization of Norbornene," *Catalysis Today* 381 (2021): 34–41.

42. E. Cristofol, "Evaluation of Various N-Phenylthiosemicarbazones as Chromogenic Reagents in Spectrophotometric Analysis," *Talanta* 38 (1991): 445–448.

43. P. I. S. Maia, A. G. d. A. Fernandes, J. J. N. Silva, et al., "Dithiocarbazate Complexes With the $[M(PPh_3)]^{2+}$ (M = Pd or Pt) Moiety: Synthesis, Characterization and Anti-*Trypanosoma cruzi* Activity," *Journal of Inorganic Biochemistry* 104 (2010): 1276–1282.

44. C. Housecroft and A. G. Sharpe, *Inorganic Chemistry*, 2nd ed. (Pearson Prentice Hall, 2005).

45. S. Cacchi and A. Arcadi, "Palladium-Catalyzed Conjugate Addition Type Reaction of Aryl Iodides with α,β-Unsaturated Ketones," *Journal of Organic Chemistry* 48 (1983): 4236–4240.

46. S. Cacchi, F. Latorre, and G. Palmieri, "The Palladium-Catalyzed Conjugate Addition Type Reaction of Aryl Iodides With α,β-Unsaturated Aldehydes," *Journal of Organometallic Chemistry* 268 (1984): c48–c51.

47. I. Czeluśniak and T. Szymańska-Buzar, "Ring-Opening Metathesis Polymerization of Norbornene and Norbornadiene by Tungsten (II) and Molybdenum (II) Complexes," *Journal of Molecular Catalysis A: Chemical* 190 (2002): 131–143.

Supporting Information

Additional supporting information can be found online in the Supporting Information section. **Figure S1:** FT-IR spectra of the $\mathbf{H_2L^{Me}}$, $\mathbf{H_2L^{Me,Me}}$ and $\mathbf{H_2L^{Ph}}$ ligand precursors. **Figure S2:** FT-IR spectra of the **mono-Pd^{Me}**, **mono-Pd^{Me,Me}** and **mono-Pd^{Ph}** complexes. **Figure S3:** FT-IR spectra of the **Ru-Pd^{Me}**, **Ru-Pd^{Me,Me}** and **Ru-Pd^{Ph}** complexes. **Figure S4:** ^{1}H NMR spectrum of $\mathbf{H_2L^{Me}}$ in DMSO-d_6. **Figure S5:** ^{1}H NMR spectrum of $\mathbf{H_2L^{Me,Me}}$ in DMSO-d_6. **Figure S6:** ^{1}H NMR spectrum of $\mathbf{H_2L^{Ph}}$ in DMSO-d_6. **Figure S7:** ^{1}H NMR spectrum of **mono-Pd^{Me}** in DMSO-d_6. **Figure S8:** ^{1}H NMR spectrum of **mono-Pd^{Me,Me}** in DMSO-d_6. **Figure S9:** ^{1}H NMR spectrum of **mono-Pd^{Ph}** in DMSO-d_6. **Figure S10:** ^{1}H NMR spectrum of **Ru-Pd^{Me}** in DMSO-d_6. **Figure S11:** ^{1}H NMR spectrum of **Ru-Pd^{Me,Me}** in DMSO-d_6. **Figure S12:** ^{1}H NMR spectrum of **Ru-Pd^{Ph}** in DMSO-d_6. **Figure S13:** $^{13}C\{^1H\}$ NMR spectrum of $\mathbf{H_2L^{Me}}$ in DMSO-d_6. **Figure S14:** $^{13}C\{^1H\}$ NMR spectrum of $\mathbf{H_2L^{Me,Me}}$ in DMSO-d_6. **Figure S15:** $^{13}C\{^1H\}$ NMR spectrum of $\mathbf{H_2L^{Ph}}$ in DMSO-d_6. **Figure S16:** $^{13}C\{^1H\}$ NMR spectrum of **mono-Pd^{Me}** in DMSO-d_6. **Figure S17:** $^{13}C\{^1H\}$ NMR spectrum of **mono-Pd^{Me,Me}** in DMSO-d_6. **Figure S18:** $^{13}C\{^1H\}$ NMR spectrum of **mono-Pd^{Ph}** in DMSO-d_6. **Figure S19:** $^{13}C\{^1H\}$ NMR spectrum of **Ru-Pd^{Me}** in DMSO-d_6. **Figure S20:** $^{13}C\{^1H\}$ NMR spectrum of **Ru-Pd^{Me,Me}** in DMSO-d_6. **Figure S21:** $^{13}C\{^1H\}$ NMR spectrum of **Ru-Pd^{Ph}** in DMSO-d_6. **Figure S22:** Intermolecular hydrogen bonds found in the crystal structure of **mono-Pd^{Me}**. [N3···O1"' = 2.919 (3) Å, N (3)–H (3)···O1"' = 145.0°] and [N6···O1" = 2.958 (3) Å, N (6)–H(6a)···O1" = 162.2°]. Symmetry operations used: (") x + 1/2, −y + 3/2, z; ("') –x, −y + 1, −z + 1. **Figure S23:** Electronic absorption spectrum of a 10^{-4} M solution of **mono-Pd^{Me}** in DMSO at 25°C. **Figure S24:** Electronic absorption spectrum of a 10^{-4} M solution of **mono-Pd^{Me,Me}** in DMSO at 25°C. **Figure S25:** Electronic absorption spectrum of a 10^{-4} M solution of **mono-Pd^{Ph}** in DMSO at 25°C. **Figure S26:** Electronic absorption spectrum and TD-DFT calculated oscillator strength (dark vertical lines) of a 10^{-4} M solution of **Ru-Pd^{Me}** in DMSO at 25°C. **Figure S27:** Electronic absorption spectrum and TD-DFT calculated oscillator strength (dark vertical lines) of a 10^{-4} M solution of **Ru-Pd^{Me,Me}** in DMSO at 25°C. **Figure S28:** Electronic absorption spectrum and TD-DFT calculated oscillator strength (dark vertical lines) of a 10^{-4} M solution of **Ru-Pd^{Ph}** in DMSO at 25°C. **Figure S29:** Cyclic voltammogram of **mono-Pd^{Me}** in DMSO at 25 ± 0.1°C vs. glassy carbon (GC) at a scan rate of 50 mV s^{-1} ([PdL] = 1 mM, [n-Bu_4NPF_6] = 0.1 M). **Figure S30:** Cyclic voltammogram of **mono-Pd^{Me,Me}** in DMSO at 25 ± 0.1°C vs. glassy carbon (GC) at a scan rate of 50 mV s^{-1} ([PdL] = 1 mM, [n-Bu_4NPF_6] = 0.1 M). **Figure S31:** Cyclic voltammogram of **mono-Pd^{Ph}** in DMSO at 25 ± 0.1°C vs. glassy carbon (GC) at a scan rate of 50 mV s^{-1} ([PdL] = 1 mM, [n-Bu4NPF_6] = 0.1 M). **Figure S32:** Cyclic voltammogram of **mono-Ru** in DMSO at 25 ± 0.1°C vs. glassy carbon (GC) at a scan rate of 50 mV s^{-1} ([Ru] = 1 mM, [n-Bu_4NPF_6] = 0.1 M). **Figure S33:** Frontier molecular orbitals (HOMO and LUMO) of **Ru-Pd^{Me}**, **Ru-Pd^{Me,Me}** and **Ru-Pd^{Ph}**. **Figure S34:** ^{1}H NMR monitoring of the reaction between **mono-Pd^{Me}** and PhI in DMSO-d_6. **Figure S35:** ^{1}H NMR monitoring of the reaction between **mono-Pd^{Me}**, NBD, and PhI in DMSO-d_6. **Figure S36:** ^{1}H NMR spectrum in $CDCl_3$ of poly(Ph-NBE) obtained via tandem catalysis.